Lake-Effect Mode and Precipitation Enhancement over the Tug Hill Plateau during OWLeS IOP2b

LEAH S. CAMPBELL, W. JAMES STEENBURGH, AND PETER G. VEALS

Department of Atmospheric Sciences, University of Utah, Salt Lake City, Utah

THEODORE W. LETCHER AND JUSTIN R. MINDER

Department of Atmospheric and Environmental Sciences, University at Albany, State University of New York, Albany, New York

(Manuscript received 25 November 2015, in final form 27 January 2016)

ABSTRACT

Improved understanding of the influence of orography on lake-effect storms is crucial for weather fore-casting in many lake-effect regions. The Tug Hill Plateau of northern New York (hereafter Tug Hill), rising 500 m above eastern Lake Ontario, experiences some of the most intense snowstorms in the world. Herein the authors investigate the enhancement of lake-effect snowfall over Tug Hill during IOP2b of the Ontario Winter Lake-effect Systems (OWLeS) field campaign. During the 24-h study period, total liquid precipitation equivalent along the axis of maximum precipitation increased from 33.5 mm at a lowland (145 m MSL) site to 62.5 mm at an upland (385 m MSL) site, the latter yielding 101.5 cm of snow. However, the ratio of upland to lowland precipitation, or orographic ratio, varied with the mode of lake-effect precipitation. Strongly orga-nized long-lake-axis parallel bands, some of which formed in association with the approach or passage of upper-level short-wave troughs, produced the highest precipitation rates but the smallest orographic ratios. Within these bands, radar echoes were deepest and strongest over Lake Ontario and the coastal lowlands and decreased in depth and median intensity over Tug Hill. In contrast, nonbanded broad-coverage periods ex-hibited the smallest precipitation rates and the largest orographic ratios, the latter reflecting an increase in the coverage and frequency of radar echoes over Tug Hill. These findings should aid operational forecasts and, given the predominance of broad-coverage lake-effect periods during the cool season, help explain the cli-matological snowfall maximum found over the Tug Hill Plateau.

1. Introduction

The apparent orographic enhancement of lake-, sea-, and ocean-effect (hereafter referred to collectively as "lake effect") precipitation occurs downstream of bod-ies of water around the world including the Laurentian Great Lakes, the Great Salt Lake, and the Sea of Japan (e.g., Magono et al. 1966; Muller 1966; Hjelmfelt 1992; Niziol et al. 1995; Steenburgh et al. 2000; Eito et al. 2005; Yamada et al. 2010; Alcott and Steenburgh 2013; Yeager et al. 2013; Veals and Steenburgh 2015). Lake-effect snowstorms can inundate urban and rural communi-ties with long-duration, intense, and often extremely localized snowfall, while orography can additionally affect the intensity, timing, and spatial distribution of precipitation. Even modest topography such as the Tug Hill Plateau (hereafter Tug Hill), which rises 500 m above the eastern shore of Lake Ontario (Fig. 1), can profoundly influence the distribution of lake-effect precipitation. Mean annual snowfall on Tug Hill ex-ceeds 700 cm in north Redfield (NR) on the western slope, more than twice that observed in the surrounding lowlands, with a record storm total of 358 cm (Veals and Steenburgh 2015). Improved understanding of the characteristics and mechanisms of this lake-effect pre-cipitation enhancement is necessary to advance pre-diction of these impactful events.

Lake-effect precipitation forms when boundary layer convection is initiated as cold air moves over a relatively warm body of water (e.g., Peace and Sykes 1966; Hozumi and Magono 1984; Niziol 1987; Kristovich and

Corresponding author address: Leah S. Campbell, Department of Atmospheric Sciences, University of Utah, 135 South 1460 East, Room 819, Salt Lake City, UT 84112.
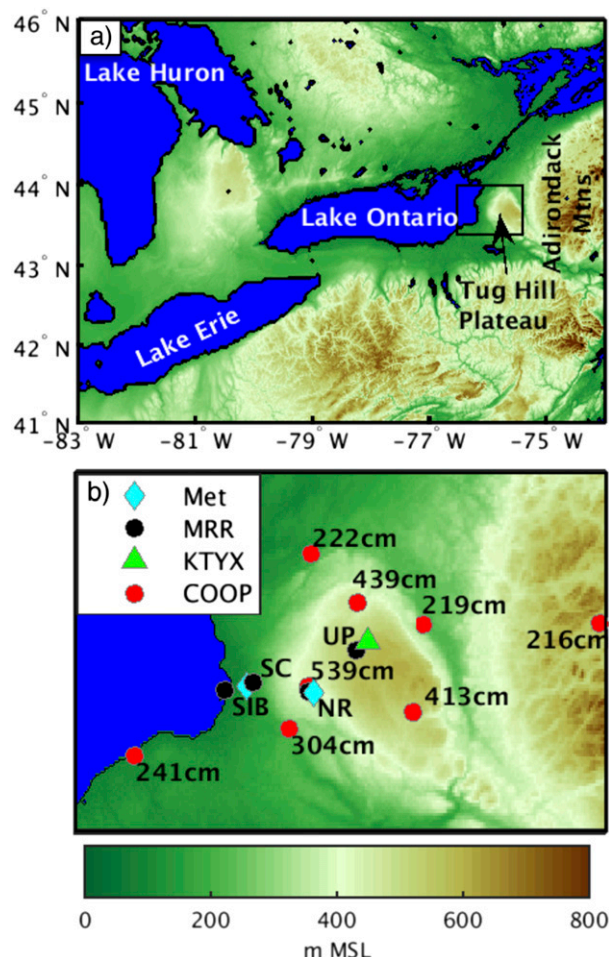E-mail: leah.campbell@utah.edu

FIG. 1. Topographic and geographic features of the (a) eastern Great Lakes and Lake Ontario and (b) Tug Hill region. Elevation (m MSL) depicted in scale at bottom. Box in (a) shows location of (b). Red circles represent COOP observing sites with annual average lake-effect snowfall (cm) from Veals and Steenburgh (2015) annotated. Black circles and blue diamonds indicate the locations of MRRs and meteorological stations (Met), respectively, at SIB, SC, NR, and UP. The green triangle represents the location of the KTYX Doppler radar.

Laird 1998). Typical lake-effect atmospheric profiles feature a moist-neutral or unstable convective boundary layer that extends to a capping stable layer or inversion at ~1–4 km above the lake surface, limiting the vertical extent of convection (Niziol 1987; Byrd et al. 1991; Kristovich et al. 2003; Schroeder et al. 2006). This convection can organize into a rich spectrum of modes (or morphologies), ranging from discrete, disorganized cells to intense mesoscale bands.

Recently, Veals and Steenburgh (2015) classified the mode of lake-effect periods over and downwind of eastern Lake Ontario using the following categories: 1) long-lake-axis parallel (LLAP) bands (e.g., Steiger et al. 2013), 2) broad coverage (e.g., Kelly 1982, 1984;

Kristovich et al. 2003), 3) hybrid (Niziol et al. 1995), 4) shoreline bands (e.g., Kelly 1986; Hjelmfelt 1990; Niziol et al. 1995), 5) mesoscale vortices (e.g., Forbes and Merritt 1984; Laird 1999), 6) lake–orographic, and 7) miscellaneous. Modeling studies have noted a connection between lake-effect mode and the ratio of wind speed to overwater fetch distance (U/L; Laird et al. 2003a,b) but this rubric has exhibited limited success when applied to observed events (Laird and Kristovich 2004). Over eastern Lake Ontario, broad coverage is the most commonly observed mode (70% of lake-effect hours), followed by LLAP concurrent with broad coverage (14%) and LLAP in isolation (10%), with the remaining categories considerably less common (Veals and Steenburgh 2015).

Climatological precipitation maxima are found over orographic features in lake-effect regions (e.g., Muller 1966; Hill 1971; Matsuura et al. 2005; Yeager et al. 2013; Veals and Steenburgh 2015), including small (~100–600 m) hills (Hjelmfelt 1992; Nakai and Endoh 1995), but few studies have specifically examined the causes of these maxima. Studies of orographic precipitation in general illustrate that the influences of orography on precipitation are multifaceted and depend on the characteristics of the larger-scale storm environment, the incident flow, the ambient stability, the size and shape of the terrain, and the time scales controlling the growth and fallout of hydrometeors [see Roe (2005), Smith (2006), Houze (2012), Colle et al. (2013), and Stoelinga et al. (2013) for reviews]. Therefore, the magnitude of orographic enhancement in lake-effect storms is likely to vary from storm to storm and may even vary within storms as a result of shifts in precipitation mode and environmental conditions.

Recently, Minder et al. (2015) used data collected by profiling radars during the Ontario Winter Lake-effect Systems (OWLeS) field campaign (Kristovich et al. 2016, manuscript submitted to *Bull. Amer. Meteor. Soc.*) to examine the evolution of lake-effect systems from the eastern shore of Lake Ontario to Tug Hill. They proposed six possible mechanisms that could affect the enhancement of lake-effect precipitation over Tug Hill: 1) orographic invigoration of convection, potentially due to the raising of the capping stable or inversion layer by orographic lift [e.g., Lackmann (2011), his Fig. 9.21], 2) increased precipitation frequency as orographic lift triggers new convective cells (e.g., Browning et al. 1974; Colle et al. 2008; Smith et al. 2009) or increases their horizontal scale (e.g., Kirshbaum and Grant 2012), 3) reduced low-level sublimation over high terrain (e.g., Murakami et al. 1994), 4) seeder–feeder (e.g., Bergeron 1965; Saito et al. 1996; Murakami et al. 1994), 5) a convective–stratiform transition similar to that observed

in mesoscale convective systems (e.g., Yuter and Houze 1995), and 6) favorable trajectories of hydrometeors generated near the shoreline and transported over downstream terrain (e.g., Alcott and Steenburgh 2013).

Minder et al. (2015) found that during 29 events observed as part of OWLeS there was no average increase in the intensity or depth of radar echoes, but rather there was an increase in their frequency and uniformity from the lowlands to Tug Hill. These findings indicate that precipitation enhancement over Tug Hill may be a result of increased persistence and/or frequency of echoes and cast doubt on the hypothesis that the orographic invigoration of lake-effect convection produces enhancement.

The purpose of the present study is to examine the enhancement of precipitation over Tug Hill during the lengthy lake-effect storm sampled during OWLeS intensive observing period 2b (IOP2b). Although Minder et al. (2015) provide a broad analysis of the effects of Tug Hill during this case, we focus here on intrastorm variations in precipitation enhancement over Tug Hill, their relationship to lake-effect precipitation mode, and the contrasting inland transition in storm characteristics responsible for periods of high and low enhancement. Our data and methods are described in section 2, with the event overview, description of precipitation enhancement over Tug Hill, and analysis of the inland evolution of vertically oriented radar profiles presented in sections 3–5. Discussion, conclusions, and suggestions for future work are provided in sections 6–7.

2. Data and methods

Our analysis concentrates on a period of intense lake-effect snowfall (0000 UTC 11 December–0000 UTC 12 December 2013) that produced the largest 24-h accumulation measured during OWLeS at the University of Utah observing site at NR (Kristovich et al. 2016, manuscript submitted to *Bull. Amer. Meteor. Soc.*). We use the Rapid Refresh (RAP; 13-km grid spacing; Benjamin et al. 2016) for regional analyses and, at times of interest, the High-Resolution Rapid Refresh (HRRR; 3-km grid spacing; Smith et al. 2008; Benjamin et al. 2016) for finescale surface analyses. The HRRR was not yet operational during the study period and was available only during the later stages of the event. GRAW GPS-based upper-air soundings launched from NR provide vertical profiles of temperature, dewpoint, and wind over Tug Hill. Additional OWLeS soundings collected at other locations add little to the analysis and are not presented here.

Radar data from the Montague, New York (KTYX), Weather Surveillance Radar-1988 Doppler (WSR-88D; see Fig. 1 for location) were obtained from the National

Climatic Data Center (NCDC) Next Generation Weather Radar (NEXRAD) archive in level II format (Crum et al. 1993), typically in ~5–6-min intervals. For plotting and analysis purposes, the 0.5° scans were interpolated to a horizontal Cartesian grid and the multielevation volume scans interpolated to a three-dimensional Cartesian grid using the Radx C++ software package for radial radar data. Regional radar composites based on data from American and Canadian operational radars were provided by the Multi-Radar Multi-Sensor (MRMS) system (Zhang et al. 2016). Although three Center for Severe Weather Research mobile radars operated during IOP2b, their deployment locations and scanning strategies provided little coverage east of Lake Ontario and are not used here. Welsh et al. (2015) describe observations collected by the University of Wyoming King Air W-band cloud radar during a portion of IOP2b, which will be the subject of a future paper.

a. Micro Rain Radars (MRRs)

To investigate transitions in storm structure over Tug Hill, we utilize observations collected along an east–west-oriented transect of observing sites deployed for OWLeS from the Lake Ontario shore through the center of the Tug Hill lake-effect snowfall maximum (Fig. 1). Four sites along the transect included a Metek Micro Rain Radar 2 (MRR; Klugmann et al. 1996): Sandy Island Beach (SIB, 75 m MSL), Sandy Creek School (SC, 175 m MSL), NR (385 m MSL), and Upper Plateau (UP, 530 m MSL). UP is located slightly north of the other three sites owing to a lack of maintained roads through the upper reaches of Tug Hill during winter (see Fig. 1 for locations). Because it was north of the region of heaviest snowfall during IOP2b, data from UP are not presented here.

The MRRs are vertically pointing frequency-modulated continuous-wave K-band (24 GHz) radars with a 2° beamwidth and 32 range gates. They operated with 200-m-range gate spacing at all four locations throughout the study period (Minder et al. 2015). We processed the raw data following Maahn and Kollias (2012), whose method is designed to work with both rain and snow and offers an improvement over the rain-specific algorithm used in generic Metek processing. The method includes noise removal, dealiasing, the calculation of equivalent radar reflectivity factor (hereafter simply "reflectivity"), removal of the top one and bottom two range gates, and averaging of the data to 60-s intervals. As discussed in Minder et al. (2015), a brief intercomparison of the MRRs used at SIB, SC, and NR revealed only a small (<3 dBZ) difference in median reflectivity profiles between the radars, so no attempt at bias correction is made owing to the uncertainties associated with a brief intercomparison.

b. Precipitation observations and estimates

Given the challenges of observing and estimating frozen precipitation rates and amounts (e.g., Rasmussen et al. 2012), we take a multipronged approach, using automated and manual liquid precipitation equivalent (LPE) and snowfall measurements as well as radar-derived LPE estimates. The automated precipitation measurements were taken at two meteorological stations located along the transect near the SC and NR MRR sites (Fig. 1). We refer to these sites using MRR site names (SC, 1.8 km west of the SC MRR at 145 m MSL, and NR, 338 m southeast of the NR MRR at 385 m MSL), even though they were not precisely collocated with the corresponding MRR. The SC site was located in a clearing surrounded by forest in the lowlands to the west (upstream) of Tug Hill, and the NR site was located in a clearing surrounded by willows and brush on the windward slope near the heart of the snowfall maximum. Each station included a Campbell Scientific HMP60 temperature and relative humidity probe, an RM Young 05103 anemometer, a heated Noah ETI weighing precipitation gauge with a single Alter-style windshield, and two automated Judd Communications snow depth sensors. One snow depth sensor measured the total depth of the snow on the ground and the other measured new snow depth on a board that was manually wiped clean every 6 h at synoptic times (0000, 0600, 1200, and 1800 UTC). Automated snow depth observations reflect quasi-instantaneous values recorded every 5 min.

At synoptic times, we also manually measured the 6-h new snow depth and LPE on two boards at both the SC and NR meteorological stations. We measured snow depth with a metric ruler at several locations on each board and averaged the observed values. LPE was obtained by weighing a core taken on the board with a Snowmetrics snowboard sampler. The values measured on the two boards were often the same, but if different, we used the average.

Although shielded weighing precipitation gauges generally perform better than heated tipping-bucket gauges (e.g., Savina et al. 2012), the presence of updrafts over the gauge orifice and the bridging of snow and ice over the gauge can still cause undercatch and/or time lags in measured precipitation amounts (Rasmussen et al. 2012). This undercatch is evident in comparisons between the manual and automated precipitation gauge measurements of 6-h accumulated LPE at SC and NR (Fig. 2). Although the manual measurements provide greater accuracy, they lack temporal resolution. As an alternative, we implement a technique described by Wüest et al. (2010) to disaggregate the 6-h manual LPE measurements

into shorter intervals using high-frequency LPE estimates derived from ~5- to 6-min 0.5° KTYX radar scans.

Radar-derived LPE estimates during snowfall are typically based on a power–law relationship (i.e., Z–S relationship):

$$Z = aS^b,$$

where Z is the radar reflectivity factor (mm^6 m^{-3}), S is the LPE rate (mm h^{-1}), and a and b are empirically derived constants (e.g., Gunn and Marshall 1958; Fujiyoshi et al. 1990; Vasiloff 2001; Rasmussen et al. 2003). Different constants may be used depending on the radar location and the size distribution/type of hydrometeors. The National Weather Service algorithm for snowfall in the Great Lakes region is

$$Z = 180S^2$$

(D. Zaff, NOAA/NWS Buffalo, 2015, personal communication); however, we use

$$Z = 75S^2,$$

which was developed by Vasiloff (2001) for snowfall in northern Utah and produces better results based on comparisons with manually measured LPE at SC and NR. When applied over the 24-h study period, this algorithm produces precipitation amounts that closely match (within 1 mm) manual observations at SC but underpredict amounts at NR by 23%. This is a closer fit to observations than the National Weather Service algorithm, which underpredicts amounts at SC by 32% and at NR by 45%.

Following Wüest et al. (2010) and Yeager et al. (2013), we calculate radar-disaggregated LPE estimates at SC and NR for each ~5–6-min period between KTYX scans using

$$G_t = \frac{S_t}{S_{6h}} G_{6h},$$

where G_t is the radar-disaggregated LPE estimate for the period beginning the minute after the previous KTYX scan and ending with the time of the current scan, S_t is the radar-derived LPE estimate for that period, S_{6h} is the 6-h radar-derived LPE estimate, and G_{6h} is the manually measured 6-h LPE. When a ~5–6-min period spans two 6-h intervals we break it into two smaller time periods, one in each 6-h interval. This method preserves the absolute accuracy of the manual observations while providing higher-frequency LPE rates. This is illustrated in Fig. 2, where 6-h radar-disaggregated LPEs derived in this manner match the
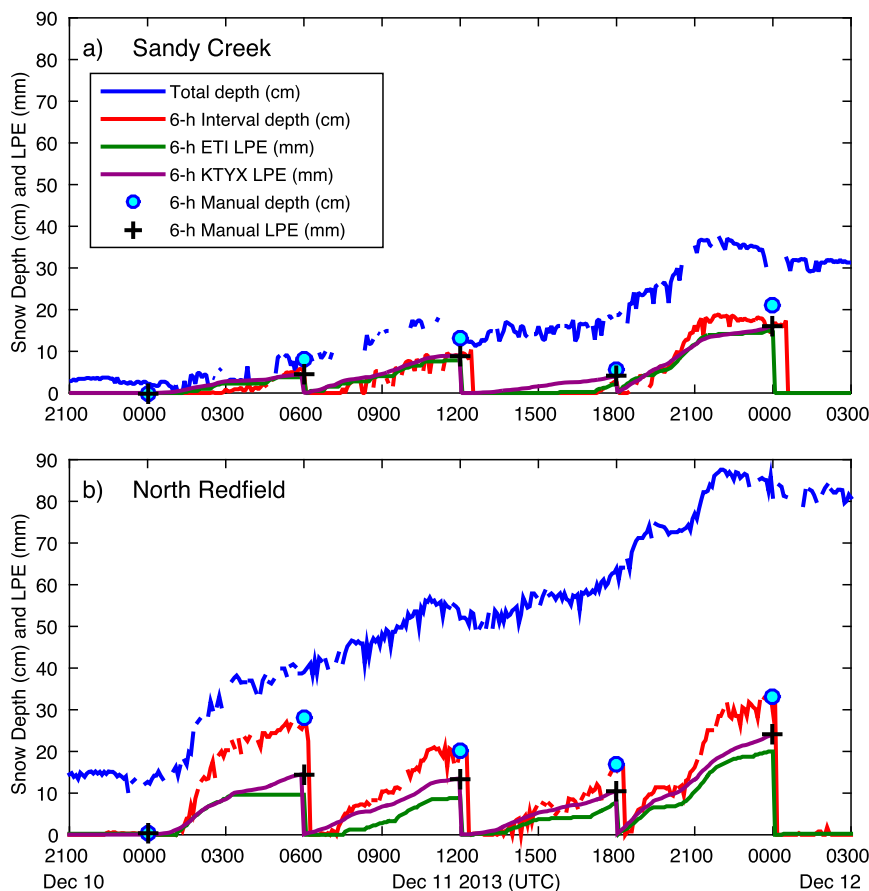
FIG. 2. Observed total snow depth (cm, blue line), automated 6-h interval snow depth (cm, red line), ETI-measured 6-h interval LPE (mm, green line), radar-disaggregated 6-h interval LPE (mm, purple line), manually measured 6-h interval depth (cm, blue circle), and manually measured 6-h interval LPE (mm, plus sign) at (a) SC and (b) NR.

manually measured LPE observed at the end of each 6-h interval. At SC, the radar-disaggregated precipitation generally matches that of the ETI gauge except from 1200 to 1800 UTC when precipitation rates were light and the ETI gauge exhibited some undercatch compared to manual measurements. At NR, the radar-disaggregated precipitation is generally larger than the ETI observations, consistent with undercatch. From 0300 to 0600 UTC, the NR ETI erroneously reported no LPE despite an increase in snow depth.

c. Lake-effect mode classification

The overall mode of lake-effect precipitation during IOP2b fluctuated between broad coverage and intense LLAP bands, with broad coverage sometimes occurring concurrently with a LLAP band (i.e., LLAP with broad coverage). Following Veals and Steenburgh (2015), we use 0.5° radar reflectivity analyses from the KTYX radar to classify the overall lake-effect mode (Figs. 3 and 4). However, we also specifically classify the mode along

the axis of the transect west of Tug Hill (i.e., west of 76°W and between 43.58° and 43.68°N along the dotted line in Fig. 3) in order to examine how precipitation features evolve along the transect.

Specifically, the mode of precipitation features along the transect (hereafter "transect mode") was classified as banded, weakly banded, nonbanded, or other (Figs. 3 and 4). During banded periods, radar echoes ≥20 dBZ formed a continuous, linear feature aligned (<15°) along the axis of the transect with length ≥50 km and horizontal aspect ratio ≥2.5:1 (e.g., Figs. 3e,g). This aspect ratio is smaller than used in previous studies categorizing boundary layer convection and lake-effect precipitation features (e.g., Weckwerth et al. 1997; Alcott et al. 2012) because we are focusing only on the area upstream of Tug Hill, which typically included only a portion of the band. During weakly banded periods, radar echoes ≥20 dBZ occurred as individual, disconnected cells connected by weaker radar echoes, were arranged linearly along the transect, and were
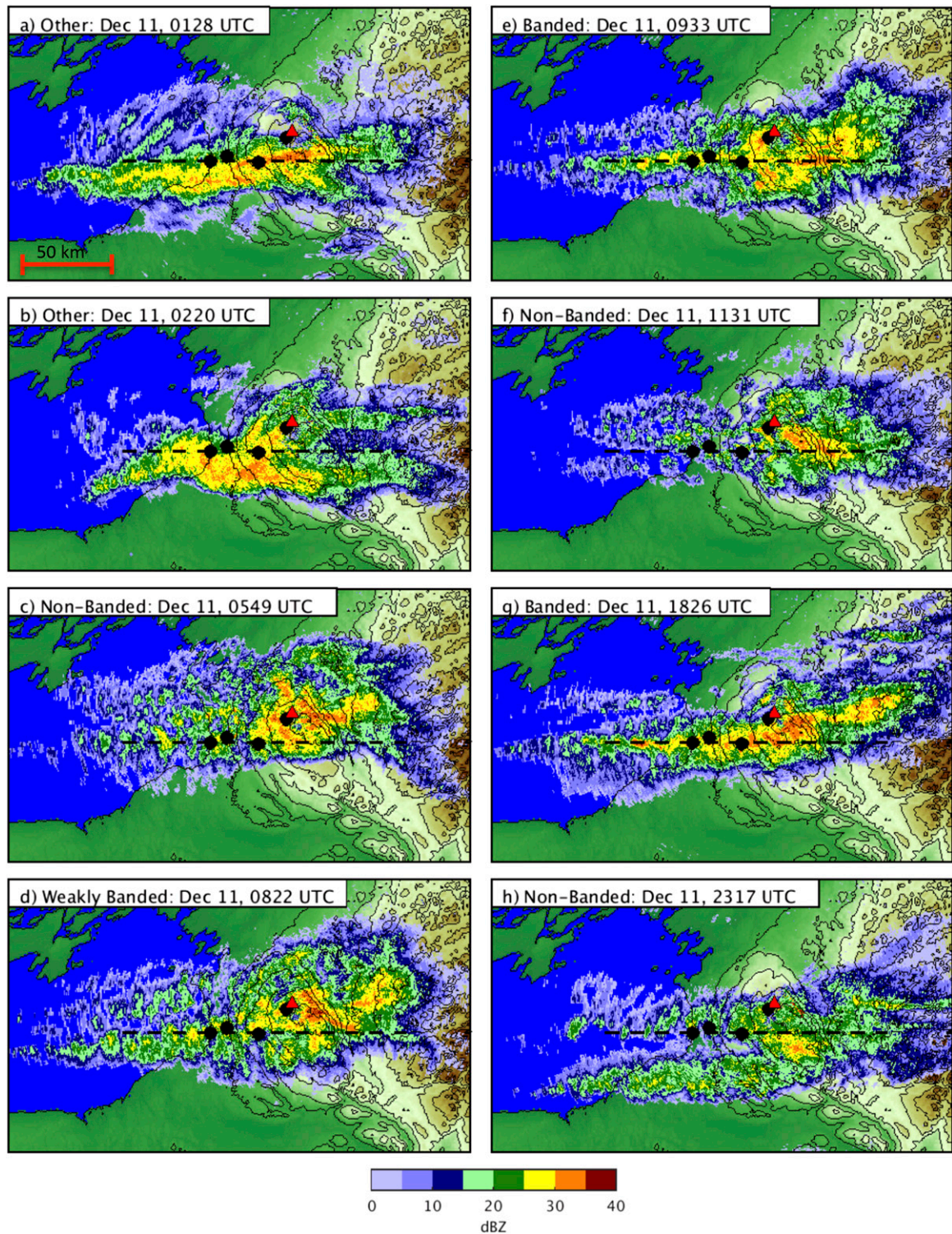
Fig. 3. KTYX 0.5° radar reflectivity (dBZ, color scale at bottom) at (a) 0128, (b) 0220, (c) 0549, (d) 0822, (e) 0933, (f) 1131, (g) 1826, and (h) 2317 UTC 11 Dec 2013. Transect mode indicated in figure labels.

Time	Overall Mode	Transect Mode	SC LPE Rate (mm/hr)	NR LPE Rate (mm/hr)	SC Accum. LPE (mm)	NR Accum. LPE (mm)	OR
0005-0049	Broad Coverage	Non-Banded	0.25	0.72	0.18	0.53	2.9
0050-0320	LLAP	Other	1.08	3.83	2.69	9.58	3.6
0321-0426	Broad Coverage	Non-Banded	0.28	1.04	0.31	1.13	3.7
0427-0459	Broad Coverage	Weakly Banded	1.19	2.57	0.64	1.37	2.2
0500-0616	Broad Coverage	Non-Banded	0.81	1.77	1.02	2.48	2.4
0617-0722	Broad Coverage	Weakly Banded	2.02	2.35	2.19	2.54	1.2
0723-0806	Broad Coverage	Non-Banded	1.35	3.12	0.97	2.24	2.3
0807-0838	Broad Coverage	Weakly Banded	0.99	0.86	0.51	0.44	0.9
0839-0900	Broad Coverage	Non-Banded	1.65	2.75	0.58	0.96	1.7
0901-0922	Broad Coverage	Weakly Banded	2.24	1.38	0.78	0.48	0.6
0923-1030	LLAP with Broad Coverage	Banded	2.23	3.2	2.49	3.57	1.4
1031-1314	Broad Coverage	Non-Banded	0.51	1.21	1.37	3.65	2.7
1315-1435	Broad Coverage	Other	0.72	2.55	0.93	3.38	3.6
1436-1654	Broad Coverage	Non-Banded	0.73	1.48	1.69	3.41	2.0
1655-1744	Broad Coverage	Weakly Banded	1.1	2.66	0.90	2.18	2.4
1745-2101	LLAP	Banded	3.62	4.25	11.83	13.88	1.2
2102-2219	LLAP with Broad Coverage	Other	1.97	5.14	2.53	6.60	2.6
2220-2358	LLAP with Broad Coverage	Non-Banded	1.15	2.5	1.89	4.08	2.2

FIG. 4. Characteristics of major lake-effect periods during IOP2b including time frame, overall mode, transect mode, radar-disaggregated LPE rate and accumulated LPE at SC and NR, and orographic ratio (OR). Shading corresponds to transect mode with red = banded, purple = weakly banded, green = nonbanded, and blue = other.

often accompanied by other disconnected radar echoes to the north and south of the transect (e.g., Fig. 3d). During nonbanded periods, individual cells with echoes ≥20 dBZ along the transect were not arranged in a linear pattern or were not connected by weaker radar echoes (e.g., Figs. 3c,f,h). The final category, other, includes periods in which the transect was in a transition zone between banded and nonbanded features (i.e., the edge of a LLAP band; e.g., Fig. 3a), so that the transect mode could not be identified unambiguously, or a banded feature was oriented obliquely so that it did not directly impact both SC and NR, precluding an along-band comparison of observed precipitation. This approach for identifying banded, weakly banded, and nonbanded periods is similar to that used for the classification of midlatitude convective systems (e.g., Gallus et al. 2008).

Each 0.5° radar scan was examined using the above-described methods and given an initial classification. When four or more consecutive scans (≥20–24 min) had a matching classification, they were identified as a period. If two periods of the same classification were separated by no more than two radar scans of a different initial classification, the two periods were combined into one with the different scans subsumed into it. There were no instances when two periods of the same classification were separated by three radar scans of a different initial classification.

3. Event overview

A broad upper-level trough persisted over the Great Lakes from 10 to 12 December, generating a 24-h period
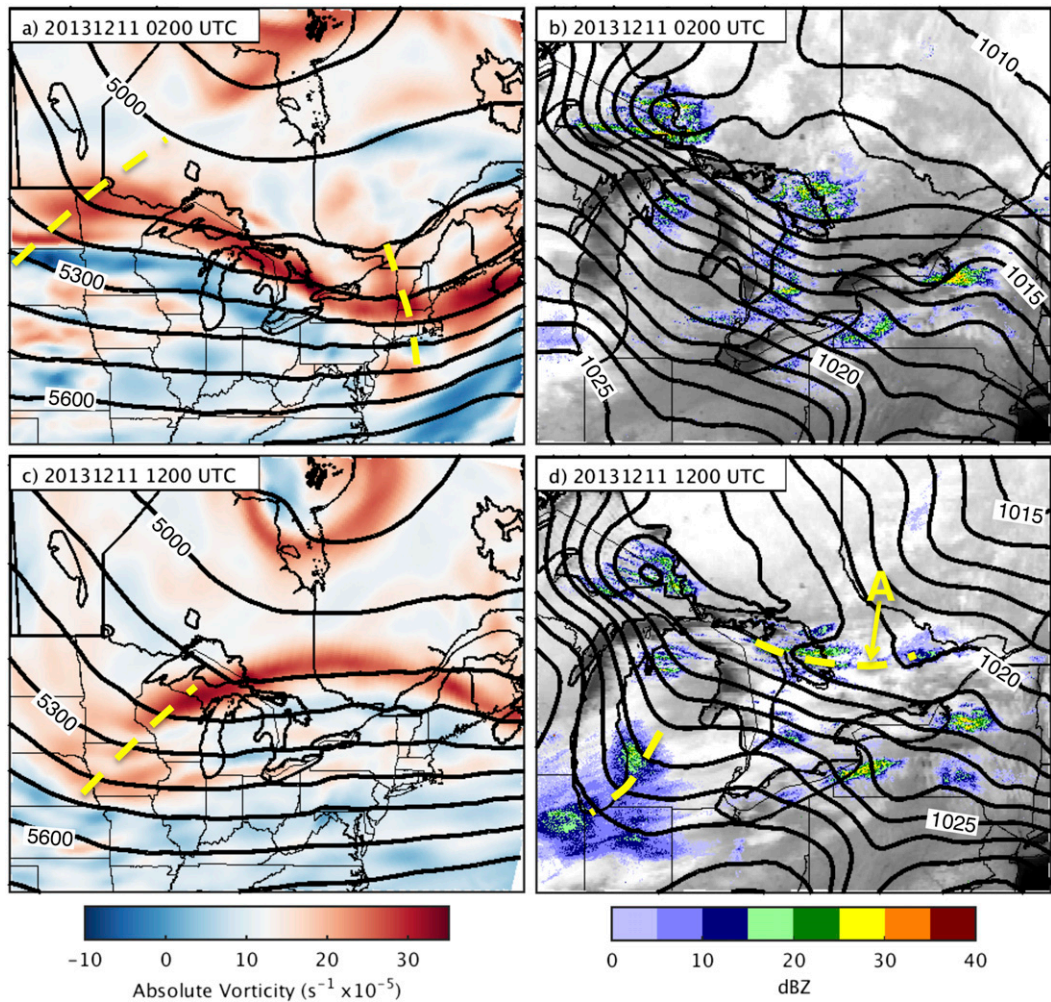
FIG. 5. (a) RAP 500-hPa geopotential height (m, contours) and absolute vorticity ($\times 10^{-5}\,\mathrm{s}^{-1}$, shaded following scale at bottom) and (b) RAP mean sea level pressure (hPa, contours), IR satellite image, and MRMS composite radar reflectivity (dBZ, shaded following scale at bottom) at 0200 UTC 11 Dec 2013. Troughs discussed in text identified with yellow dashed lines. (c),(d) As in (a),(b), but at 1200 UTC.

(0000 UTC 11 December to 0000 UTC 12 December) of lake-effect snow over Tug Hill. The period began with the passage of a 500-hPa short-wave trough (Fig. 5a), with weak broad-coverage lake effect transitioning to an LLAP band that hovered just south of the transect [e.g., 0128 UTC 11 December (Fig. 3a); subsequent dates 11 December unless otherwise specified]. By 0200 UTC, the short-wave trough axis was just east of Lake Ontario and broad west-northwest (WNW) geostrophic flow extended from the surface to 500 hPa across the eastern and central Great Lakes (Figs. 5a,b). A sounding released from NR at 0215 UTC shows a nearly saturated, moist-neutral convective boundary layer capped by a stable layer based at ~650 hPa, with boundary layer winds backing with height from WNW to west (W) (Fig. 6a). At ~0220 UTC, the LLAP band took on a

transitional, wavelike shape (e.g., Fig. 3b) before decaying by 0320 UTC. Mean MRR echo tops at SC and NR were ~2800–3000 m MSL between ~0100 and 0300 UTC, consistent with the boundary layer depth and the associated layer of weak stability inferred from RAP equivalent potential temperature (θ_e) time–height analyses (Fig. 7). During this period, precipitation rates were among the highest of the event at NR but remained relatively low at SC (Fig. 2), which was frequently located north of the strongest portion of the LLAP band (e.g., Fig. 3a). For this reason, we classify the transect mode during this period (0050–0320 UTC; Fig. 4) as ''other'' since contrasts in precipitation between SC and NR were due to band orientation rather than inland or orographic enhancement.

From 0320 to 1030 UTC, zonal 500-hPa flow prevailed over Lake Ontario with little change in the large-scale
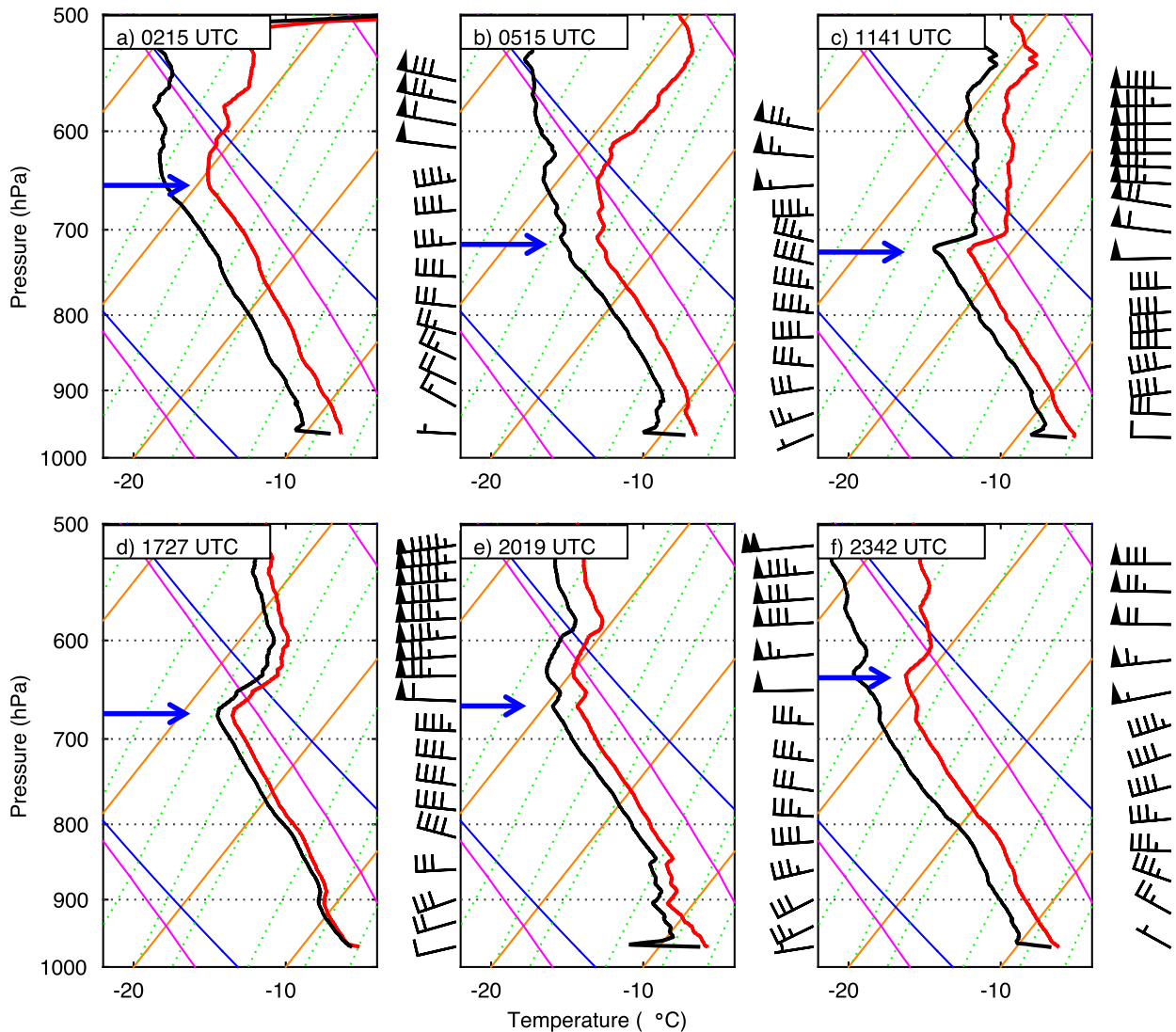
FIG. 6. Skew T–log$p$ diagrams [temperature (red), dewpoint (black), and wind barbs (full and half barbs denote 5 and 2.5 m s^{-1}, respectively)] at NR for (a) 0215, (b) 0515, (c) 1141, (d) 1727, (e) 2019, and (f) 2342 UTC 11 Dec 2013. Blue arrows denote subjectively identified convective boundary layer top height.

surface pattern (not shown). Midtropospheric warming resulted in a shallower convective boundary layer that extended to only ~710 hPa by 0515 UTC, about 60 hPa lower than at 0215 UTC (cf. Figs. 6a,b and 7). Concurrently, precipitation rates decreased (Fig. 2) and MRR echo tops lowered over SC and NR (Fig. 7). From 0321 to 0922 UTC broad coverage predominated the overall mode, with vacillations from nonbanded [e.g., 0549 UTC (Fig. 3c)] to weakly banded [e.g., 0833 UTC (Fig. 3d)] transect modes. Radar echoes were typically scattered and disorganized over eastern Lake Ontario and the adjoining lowlands, but coverage increased and became more widespread and persistent over Tug Hill (e.g., Figs. 3c,d). From 0923 to 1030 UTC, a

short-lived, narrow LLAP band formed over the transect that was surrounded by weaker, disorganized precipitation features that similarly increased in coverage over Tug Hill [e.g., 0933 UTC (Fig. 3e)], although MRR echo tops remained relatively low (Fig. 7).

By 1200 UTC, Lake Ontario was beneath broad, very-low-amplitude ridging with an upstream short-wave trough moving over the upper Great Lakes region (Fig. 5c). Surface troughs were evident east of Lakes Huron (labeled A) and Michigan (Fig. 5d). MRR echoes at SC and NR were shallow with brief periods of no returns between ~1030 and 1300 UTC (Fig. 7). In the 1141 UTC sounding, the convective boundary layer over NR extended to only 720 hPa with nearly unidirectional
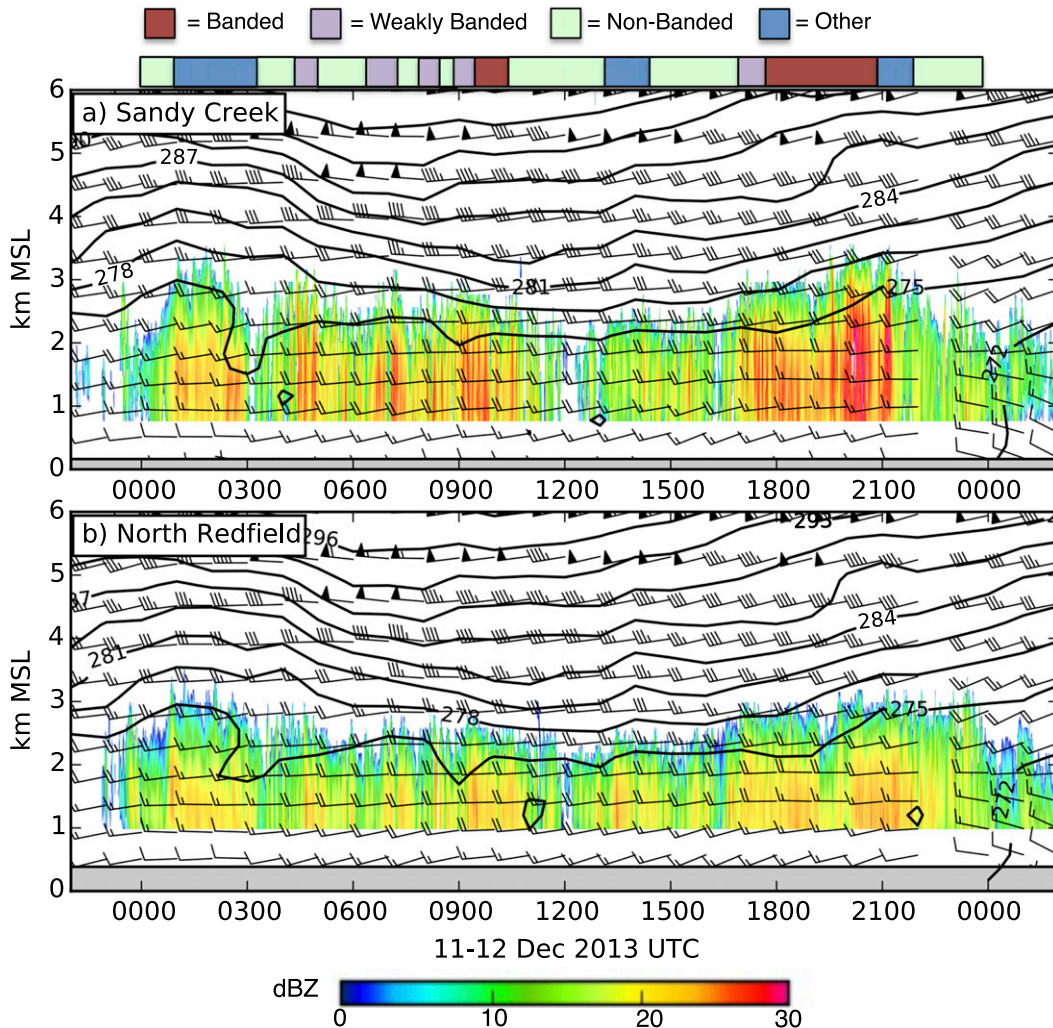
FIG. 7. Time–height analysis of MRR radar reflectivity (dBZ, shaded following scale at bottom), RAP θ_e (K, contours every 3 K), and RAP wind (full and half barbs denote 5 and 2.5 m s^{-1}, respectively) at (a) SC and (b) NR. RAP analysis not available at 2200 UTC 11 Dec 2013. Indicator bar colors denote transect mode as in Fig. 4.

westerly flow (Fig. 6c). Precipitation rates were the lowest of the event at SC and were also light at NR (Fig. 4). Broad coverage with vacillations from non-banded [e.g., 1131 UTC (Fig. 3f)] to weakly banded transect modes prevailed from 1031 to 1744 UTC (not shown). We classify the transect mode from 1315 to 1435 UTC as other because the transect was on the edge of a weak band and we could not unambiguously define the mode (not shown).

By 1800 UTC, the upstream 500-hPa short-wave trough was moving over Lake Michigan (Fig. 8a). At the surface, trough A was moving southward and was just north of Lake Ontario, with a zonally oriented trough (labeled B) extending from Lake Michigan across southern Michigan and southwest Ontario (Fig. 8b). A precipitation band accompanied each of

these troughs (Fig. 8b) as well as a pronounced wind shift and band of convergence, as illustrated by higher-resolution HRRR analyses (Fig. 9a). The HRRR also resolved the presumably lake-driven convergence over and downstream of Lakes Ontario (labeled C) and Erie (labeled D). Convergence associated with trough B appeared to connect quasi continuously with the lake-driven convergence over Lake Ontario (Fig. 9a). Also during this period, midtropospheric temperatures decreased and the convective boundary layer over NR deepened to ~670 hPa at 1727 UTC and ~660 hPa at 2019 UTC (cf. Figs. 6c,d,e). Boundary layer winds at both times veered weakly with height from west-southwest (WSW) to WNW (Figs. 6d,e).

An intense LLAP band formed at ~1745 UTC and extended over the transect through 2101 UTC [e.g., 1826 UTC
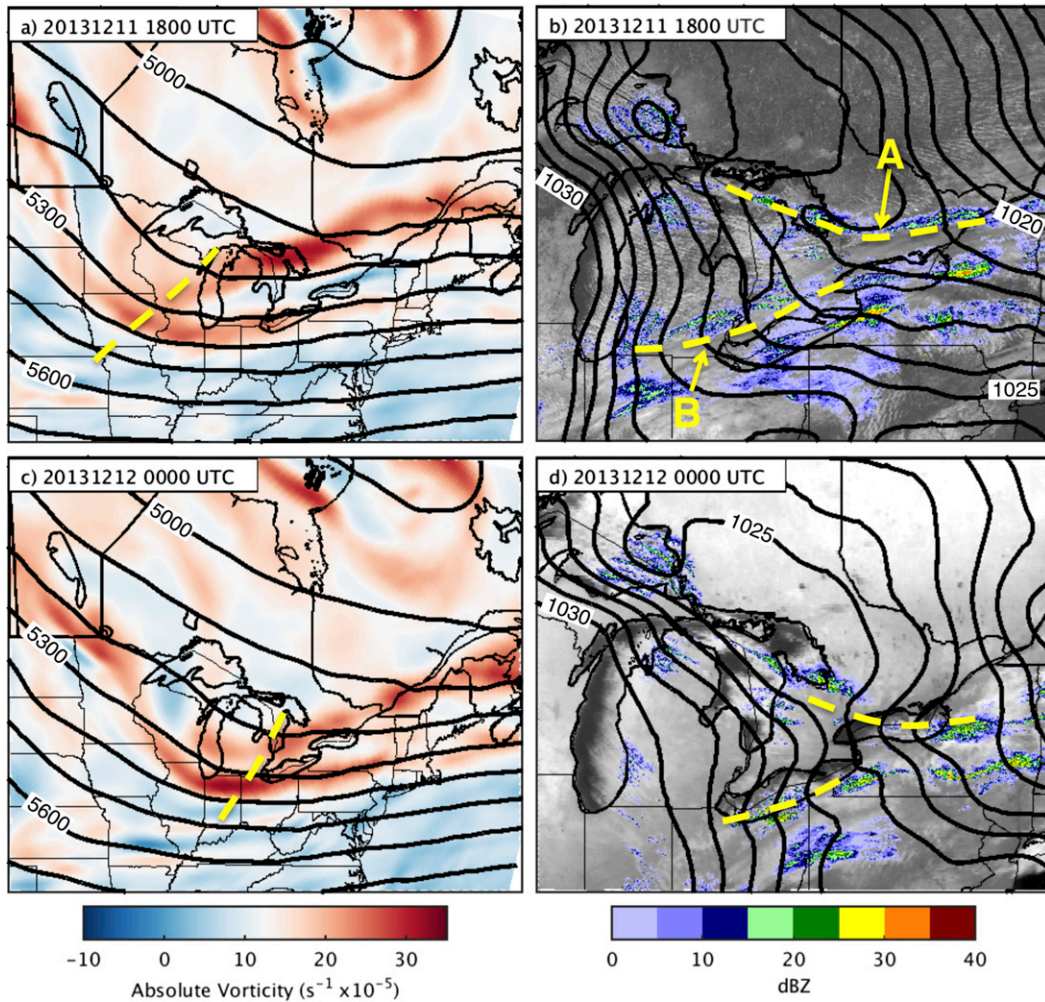
FIG. 8. As in Fig. 5, but for (a),(b) 1800 UTC 11 Dec and (c),(d) 0000 UTC 12 Dec 2013.

(Fig. 3g)], producing the largest precipitation rates of the event at both SC and NR (Fig. 4). Concurrently, MRR echo tops rose to >3000 m MSL at SC and >2800 m MSL at NR (Fig. 7). Although not examined in detail here, the development of the intense LLAP band during this period appears to be closely related to large-scale kinematic and thermodynamic changes occurring over the Great Lakes region and occurred shortly following or concurrently with the development and intensification of surface troughs A and B and associated convergence zones. Niziol et al. (1995) discuss similar modulation of lake-effect storms by upper-level and surface troughs.

By 0000 UTC 12 December, the 500-hPa short-wave trough axis was over Lake Huron (Fig. 8c) and surface trough A was over Lake Ontario (Fig. 8d). The convergence associated with trough A was now indistinguishable from the lake-driven convergence over Lake Ontario, which migrated southward to the south

shore as the low-level wind shifted to WNW (Fig. 9b, cf. Figs. 6e,f for wind shift). A similar evolution occurred over Lake Erie as trough B sagged southward (cf. Figs. 9a,b). The western end of the LLAP band began to progress south between 2100 and 2219 UTC, positioning it with an oblique angle to the transect (not shown) and gradually moving the entire band southward. From 2220 to 2358 UTC the main LLAP band was south of Tug Hill, but nonbanded and weakly banded convection continued over the transect, at times approaching a double-banded mode [e.g., 2317 UTC (Fig. 3h)]. MRR echo tops steadily lowered between 2100 and 2358 UTC (Fig. 7), remaining low in the early hours of 12 December, until precipitation ended around 0300 UTC 12 December.

4. Precipitation enhancement over Tug Hill

The areal extent of precipitation produced during IOP2b covered a ~50-km-wide corridor that extended
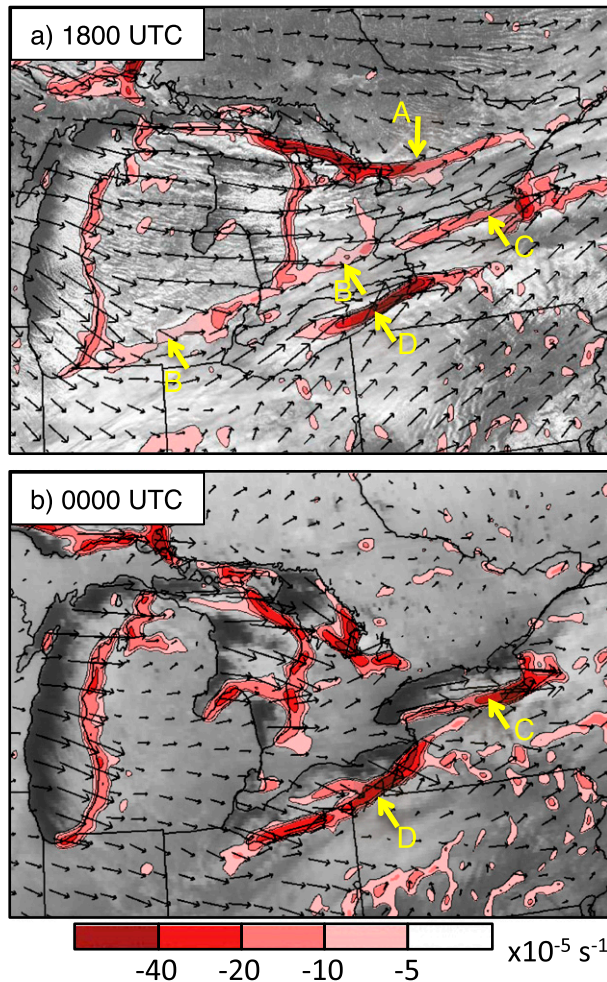
FIG. 9. HRRR 10-m wind vectors and divergence ($\times 10^{-5}\,\mathrm{s}^{-1}$, shaded following scale at bottom) overlaid on visible or infrared satellite imagery at (a) 1800 UTC 11 Dec and (b) 0000 UTC 12 Dec 2013. Wind vectors thinned and divergence smoothed using a cowbell spectral filter (Barnes et al. 1996) for clarity. Wind shifts and convergence zones discussed in text are identified with labeled arrows.
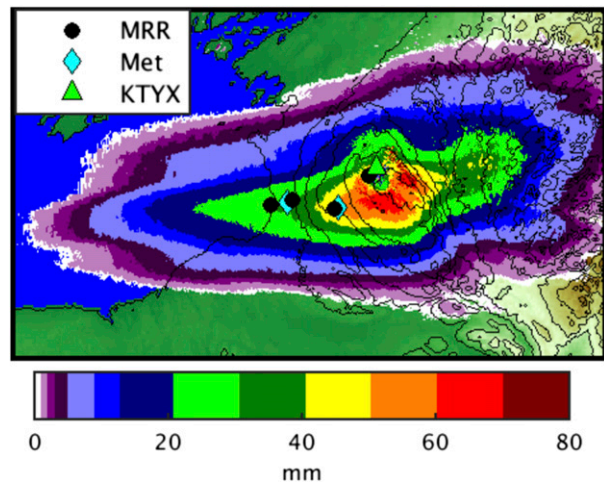

FIG. 10. Radar-derived LPE (mm, shaded following scale at bottom) from 0000 UTC 11 Dec to 0000 UTC 12 Dec 2013. Locations of MRRs (black circles), meteorological stations (blue diamonds), and the KTYX radar (green triangle) denoted with symbols.

from the eastern shore of Lake Ontario across Tug Hill to the western Adirondacks (Fig. 10). The precipitation maximum was centered over Tug Hill, with a pronounced precipitation gradient from the shoreline to the upper elevations along the axis of maximum precipitation. The band of maximum precipitation also broadened with inland extent, was widest over Tug Hill, and contracted in the lee where it continued east-northeast (ENE) into the western Adirondacks. Based on manual measurements collected every 6 h, snowfall (LPE) increased from 47.8 cm (33.5 mm) at SC to 101.5 cm (62.5 mm) at NR (Fig. 2). Thus, the mean ratio of upland to lowland precipitation (i.e., NR LPE/SC LPE), or orographic ratio, was 1.9 for the 24-h study

period and 1.6 when excluding transect mode periods categorized as other.

The orographic ratio was lowest, however, during banded periods (1.2) and highest during nonbanded periods (2.3; Fig. 11; not including other periods). The spatial distribution of echo frequencies $\geq 10\,\mathrm{dB}Z$ during banded and nonbanded periods helps illustrate important changes in storm characteristics between the two transect modes (Fig. 12). During banded periods, an elongated region of >90% echo frequencies stretched eastward from Lake Ontario and broadened over Tug Hill (Fig. 12a). A cross section through the axis of highest echo frequency (identified with white dashed line in plan view plots) shows a steady decrease in the height of the ≥ 10-dBZ frequency gradient between the shoreline and the lee of Tug Hill during these banded periods (Fig. 12b). This is consistent with a decrease in the depth of precipitation features, in contrast to the deepening one might expect if there was a lifting of the capping stable layer or inversion and an invigoration of convection by orographic lift.

In contrast, nonbanded periods exhibited a pronounced east-to-west frequency gradient between the shoreline (~40% frequency) and the western (windward) slope (>90% frequency), with a broad shield of frequent echoes $\geq 10\,\mathrm{dB}Z$ over Tug Hill (Fig. 12c). This gradient is also evident in the cross-section view as the ≥ 10-dBZ echo frequencies systematically increase between the shoreline and the upper elevations of Tug Hill (Fig. 12d). The cross section also suggests that precipitation features during nonbanded periods were
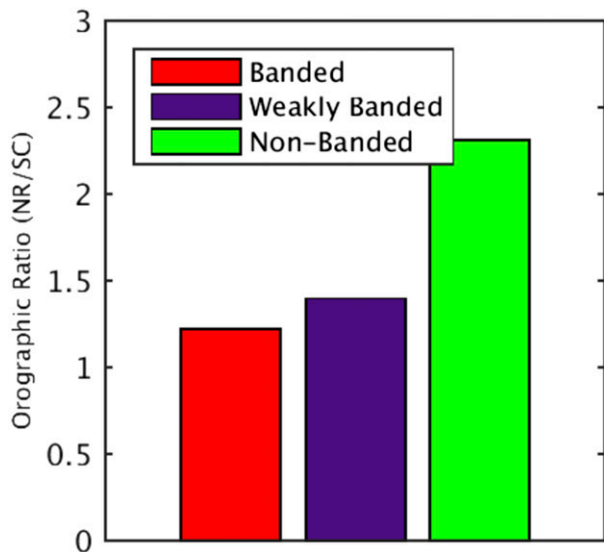
FIG. 11. Orographic ratio (NR LPE/SC LPE) during banded, weakly banded, and nonbanded periods.

relatively shallow, as the majority of $\geq$10-dBZ echoes are contained below ~2500 m MSL both over the lake and Tug Hill (Fig. 12d). It is likely that offshore echoes were affected by overshooting and/or beam filling

particularly when radar echoes were shallow, so some of the deeper returns apparent on the western edge of this cross section may be an artifact.

Although banded periods had the lowest orographic ratios (Fig. 11), they produced the highest mean precipitation rates at both locations (3.3 mm h^{-1} at SC and 4.0 mm h^{-1} at NR; Fig. 13a). In contrast, nonbanded periods produced the largest orographic ratios (Fig. 11), but mean precipitation rates that were more than 4 times lower at SC (0.8 mm h^{-1}) and more than 2 times lower at NR (1.8 mm h^{-1}) than observed during banded periods (Fig. 13a). However, nonbanded periods were the most frequent mode observed along the transect (10.1 h), followed by other (6.2 h), banded (4.4 h), and weakly banded (3.3 h). At SC, banded modes produced almost twice as much accumulated precipitation (14.3 mm) as nonbanded modes (8.0 mm; 13b), but at NR banded modes produced less precipitation (17.5 mm) than nonbanded modes (18.5 mm; Fig. 13b). These findings indicate that SC owes the majority of its accumulated precipitation to banded periods, whereas NR received a large contribution from nonbanded periods. Therefore, the prevalence of nonbanded periods contributed to the large overall orographic ratio.
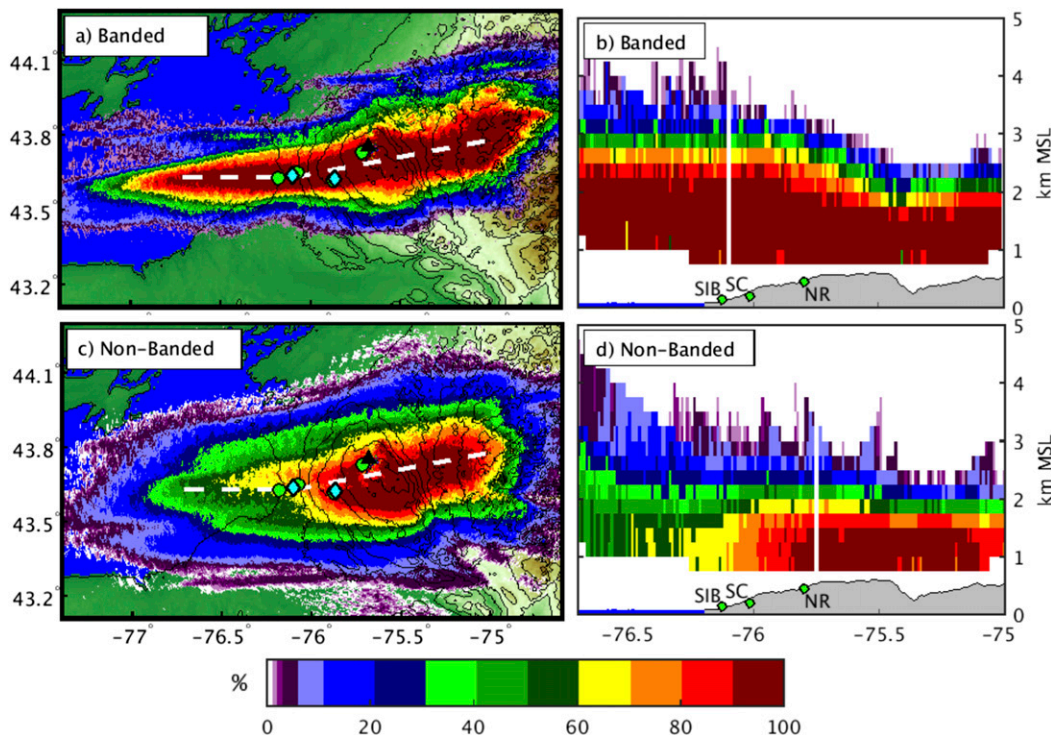

FIG. 12. Frequency of radar reflectivity $\geq$10 dBZ (shaded following scale at bottom) during banded periods in (a) KTYX 0.5° elevation scans and (b) within a cross section [white dashed line shown in (a)] through KTYX volume scans. (c),(d) As in (a),(b), but during nonbanded periods.
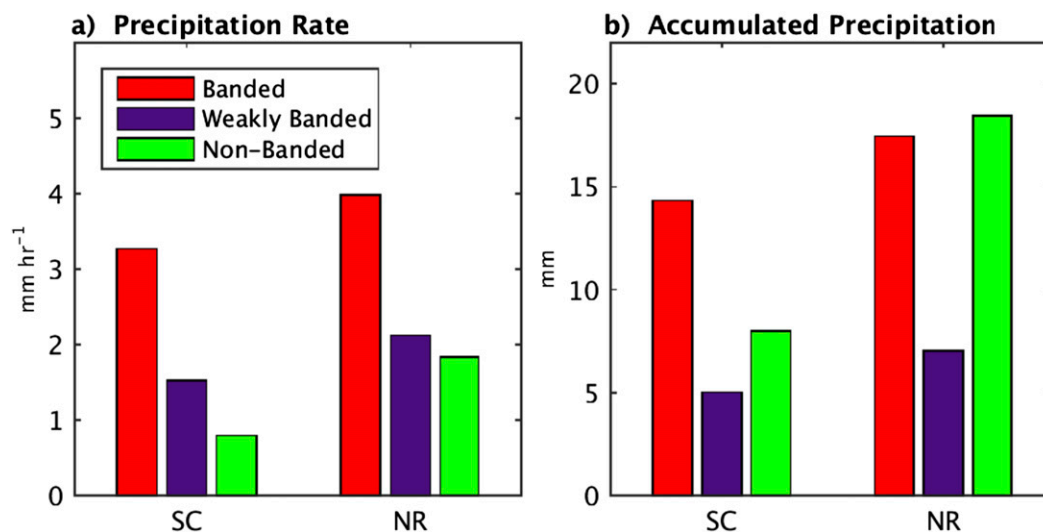
FIG. 13. (a) Mean radar-disaggregated precipitation rate (mm h^{-1}) at SC and NR during banded (red), weakly banded (purple), and nonbanded (green) periods. (b) Total accumulated precipitation (mm) at SC and NR during banded (red), weakly banded (purple), and nonbanded (green) periods.

5. Inland evolution of MRR profiles

The transect of MRR profiling radars (described in section 2b; for locations, see Fig. 1) provides vertical profiles of reflectivity, Doppler velocity, and spectral width at SIB, SC, and NR at high temporal and vertical resolution. In an earlier study investigating the evolution of precipitation structures along the MRR transect, Minder et al. (2015) found that during IOP2b as a whole there was a weakening of convective vigor and turbulent motions and no increase in echo depth with inland extent. However, radar reflectivity echoes were more frequent and uniform over NR than over SC, consistent with the Tug Hill precipitation maximum. We further this analysis by examining the differences in vertical structure along the transect between banded and nonbanded periods. Similar to Minder et al. (2015), we employ contoured frequency by altitude diagrams (CFADs; Yuter and Houze 1995), which display stacked histograms of reflectivity (1.5 dBZ bins), velocity (0.1 m s^{-1} bins), and spectral width (0.1 m s^{-1} bins) frequency distributions above the SIB, SC, and NR MRRs.

At all three sites, banded periods feature a shift in CFAD values toward higher reflectivity with decreasing height to broad maxima at 0.9–1.5 km MSL, consistent with the growth of falling hydrometeors (Figs. 14a–c). At SIB and SC, the median reflectivity is ~10 dBZ at 3.0 km MSL, below which the median reflectivity maximizes at 25.3 dBZ. Although the overall structure of the NR CFAD is similar to that at SIB and SC, there are some important differences, which can be more easily

discerned by directly comparing the median and interquartile range (IQR) reflectivity profiles (Fig. 15a). In particular, at NR, the median and IQR echo magnitudes and altitudes are ~4 dBZ weaker and ~500 m lower, respectively, than at SIB, with a smaller IQR above 2.0 km MSL. These results are consistent with a shift to shallower echoes moving from the Lake Ontario shore to Tug Hill, as suggested by the KTYX cross section (Fig. 12b). The transition to weaker reflectivities, however, is somewhat counterintuitive given the small increase in observed precipitation from SC to NR during banded periods. The causes for this inconsistency are unclear but could reflect factors such as calibration, a shift in hydrometeor size into or within the Mie scattering regime, or contrasts in hydrometeor evolution below the lowest range gate. In the case of the latter, the strong decrease in median reflectivity below 1.0 km MSL at SIB could reflect the influence of low-level sublimation and/or low-level hydrometeor growth if in the Mie scattering regime. Unfortunately, since the lowest two range gates are unusable, we were unable to observe the lowest 600 m AGL using the MRRs.

A direct comparison of Doppler velocity and spectral width profiles further highlights the transition in storm characteristics from the Lake Ontario shore to Tug Hill during these banded periods. At SIB, the median Doppler velocity (positive indicates downward) increases with decreasing height from 0.15 m s^{-1} at 3.5 km MSL to 1.2 m s^{-1} at the lowest range gate, with an IQR of ~1.0 m s^{-1} for much of the profile (Fig. 15b). Given that the Doppler velocity reflects the vertical wind combined with the hydrometeor fall speed, two possible
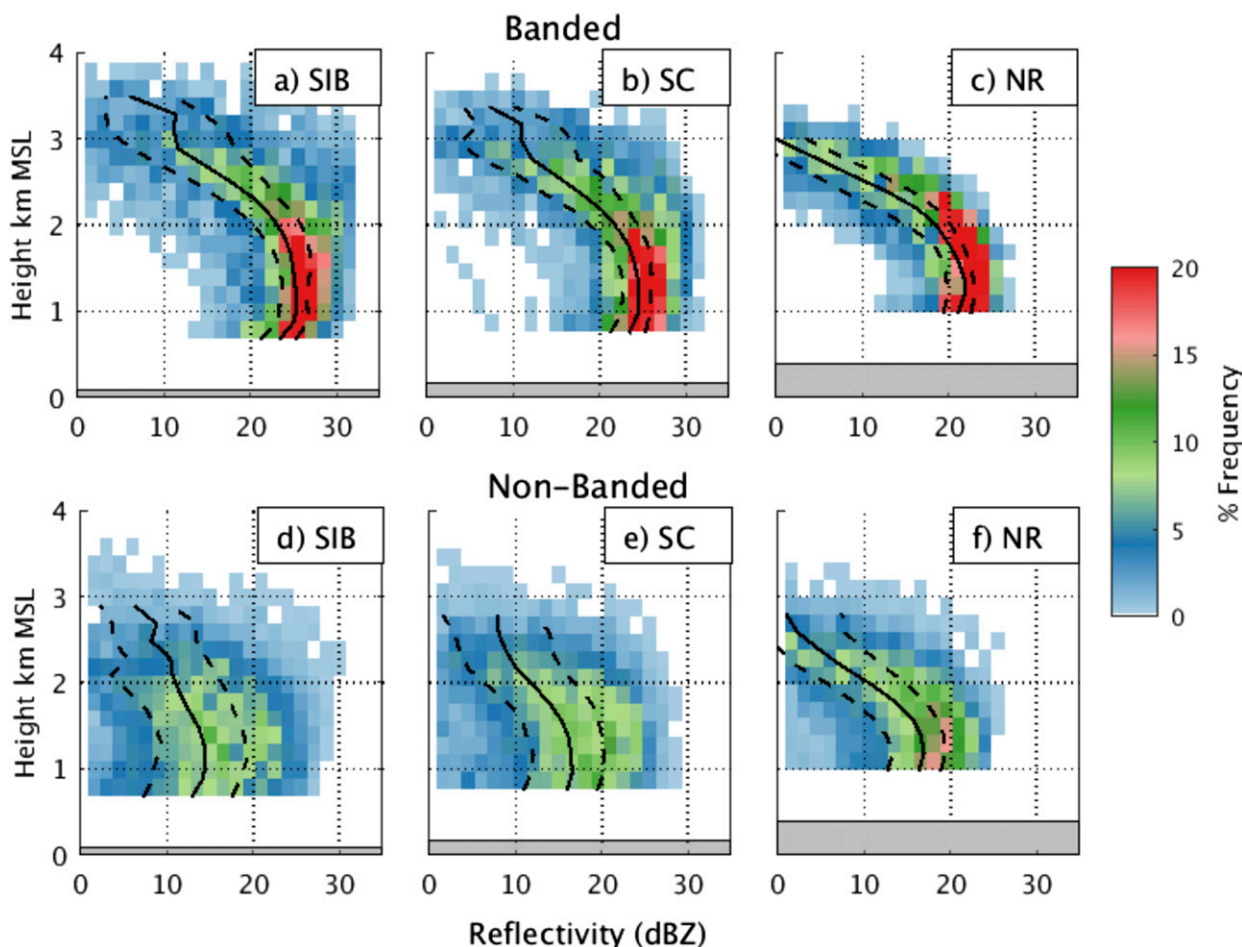
FIG. 14. MRR reflectivity CFADs (shaded following scale at right) during banded periods at (a) SIB, (b) SC, and (c) NR. (d)–(f) As in (a)–(c), but for nonbanded periods. Solid line represents the median and dashed lines represent the lower and upper quartiles.

contributors to this profile are 1) an increase in hydrometeor fall speed toward the surface if vertical motions are weak or 2) a countering of hydrometeor fall speed aloft by frequent convective updrafts. The latter is consistent with the intense, strongly organized lake-effect bands observed during these banded periods. In contrast, Doppler velocities at NR are more uniform with height and the IQR is smaller than at SIB (Fig. 15b). This profile is similar to that observed in stratiform regions of mesoscale convective systems, where upward vertical motion is strong enough to allow for vapor deposition but weak enough to let hydrometeors drift downward (Yuter and Houze 1995; Houze 1997). Additionally, the spectral width is weaker and has a narrower IQR at NR than at SIB, consistent with a decline in turbulence and/or variance in hydrometeor fall speed (Fig. 15c). Collectively, these results suggest a decrease in convective vigor and turbulence from the Lake Ontario shore to Tug Hill, as also observed by the

University of Wyoming King Air W-band cloud radar from 1905 to 2105 UTC (Welsh et al. 2015).

In contrast to the high reflectivities and small IQRs observed during banded periods, reflectivity profiles during nonbanded periods feature weaker reflectivities and larger IQRs at the three sites (cf. Figs. 14a–c, Figs. 14d–f). At SIB, median reflectivities increase toward the ground from ~5 dBZ just below 3.0 km to a maximum of 14.5 dBZ at 1.1 km MSL. The IQR is relatively wide, spanning 10 dBZ below 2.0 km MSL (Fig. 14d), implying large variability in echo strength and intermittent, showery precipitation. A similar signal is apparent at SC, although a slight increase in the median reflectivity and decrease in the IQR below 2.0 km MSL indicates slightly steadier, stronger precipitation than at SIB (Fig. 14e). From SC to NR there is an increase in reflectivity below 1.7 km MSL (cf. Figs. 14d–f), which is more easily discerned in the direct comparison in Fig. 15d. Collectively, these results are consistent
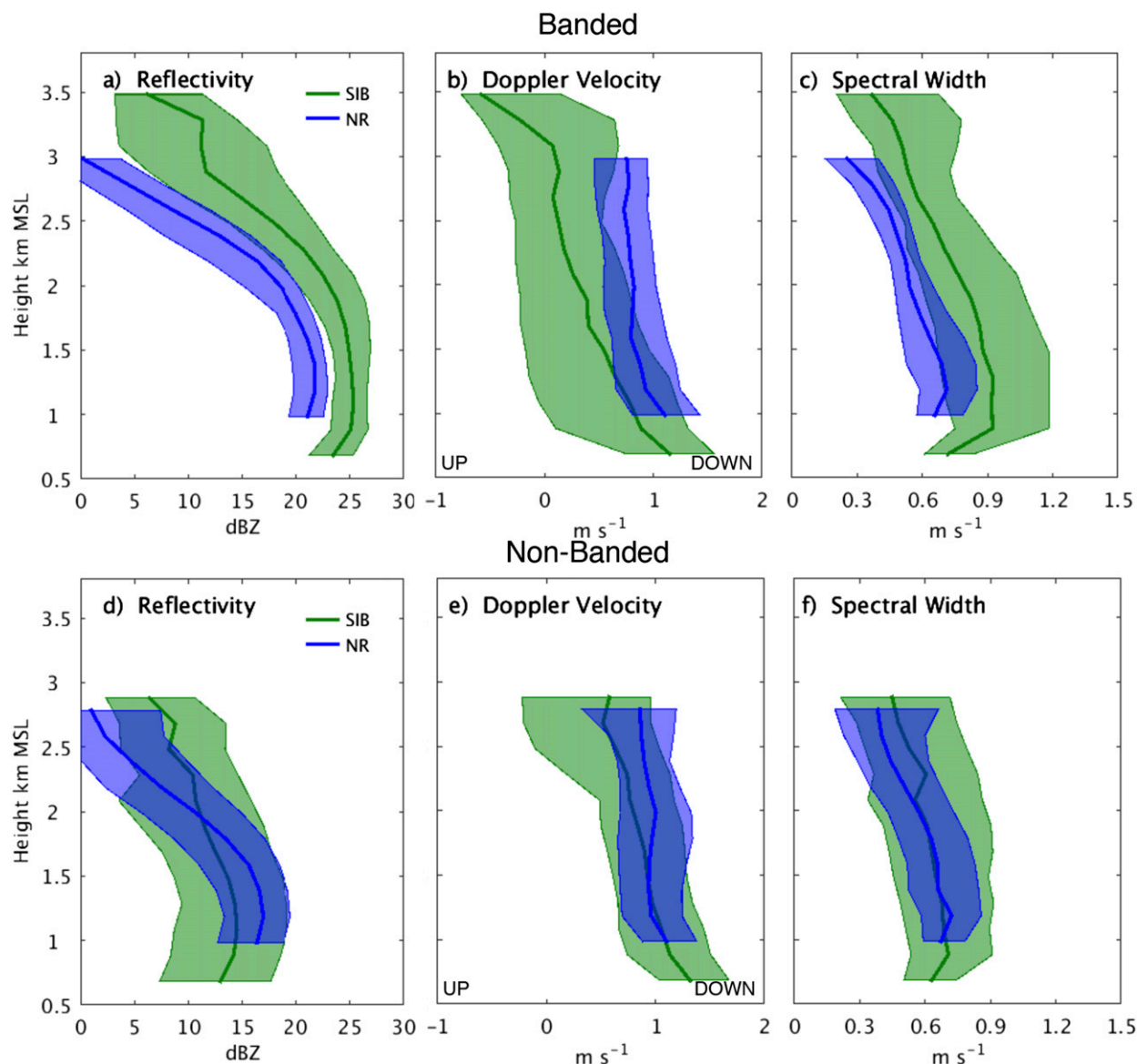
FIG. 15. Comparison of median (middle line) and interquartile range (color fill) of MRR (a) reflectivity, (b) Doppler velocity, and (c) spectral width at SIB (green) and NR (blue) during banded periods. (d)–(f). As in (a)–(c), but during nonbanded periods.

with a shift toward stronger, more persistent echoes over Tug Hill and the large orographic ratio of 2.3 observed during nonbanded periods.

Median Doppler velocities at SIB increase with decreasing height during nonbanded periods to a maximum at the lowest range gate (Fig. 15e). Although this increase toward the ground is also seen during banded periods, the median Doppler velocity during nonbanded periods is as much as $0.5 \, \mathrm{m \, s^{-1}}$ larger at 3.1 km MSL than during banded periods. This, along with a smaller IQR and smaller median spectral widths, suggests weaker, more intermittent convection. In contrast to the structure

observed at SIB, the Doppler velocity and spectral width profiles at NR are fairly uniform with height and are similar in structure and magnitude to that observed during banded periods. These results illustrate that there is a decrease in convective vigor over Tug Hill during both nonbanded and banded periods, consistent with the general result of Minder et al. (2015) over 29 OWLeS events, even though the convective vigor at the Lake Ontario shore is weaker during nonbanded periods. Therefore, mechanisms other than the deepening and invigoration of convection must be responsible for the large orographic ratios observed during nonbanded periods.

6. Discussion

While the causes for the variations in lake-effect mode observed in this event are not explored in depth here, the strongest LLAP bands occurred with the passage or approach of upper-level shortwave troughs, a phenomenon also noted by Niziol et al. (1995). Cooler midtropospheric temperatures associated with these troughs most likely enabled deeper lake-effect convection (e.g., Byrd et al. 1991; Reinking et al. 1993) and thus a stronger circulation within the band, leading to invigorated mesoscale convergence. In addition, the most intense LLAP-band period occurred shortly following or concurrently with the development of surface troughs and precipitation bands east of Lake Huron and east of Lake Michigan (over southern Michigan and southwest Ontario). The convergence associated with the latter connected quasi continuously with convergence over Lake Ontario. Whether or not this is coincidental or causal is unclear. Although most prior research emphasizes the role of land–breeze convergence in LLAP-band development (Peace and Sykes 1966; Passarelli and Braham 1981; Braham 1983; Hjelmfelt 1990; Niziol et al. 1995; Steenburgh and Onton 2001; Onton and Steenburgh 2001; Steiger et al. 2013), convergence associated with regional-scale processes may have played a role in the development of the LLAP bands during IOP2b.

We hypothesize that the strong mesoscale convergence associated with such LLAP bands serves as a locus for organizing convection, effectively releasing CAPE regardless of terrain effect. Accordingly, during banded periods, the depth and vigor of convection was largest near the lake shore and decreased inland to Tug Hill (Figs. 13, 14a–c, 15). These factors enabled precipitation rates to be nearly as high in the coastal lowlands as over Tug Hill (Fig. 13a). We note, however, that there is a weak downstream broadening of the LLAP bands, so that snowfall occurs over a larger area as one moves inland over Tug Hill.

In contrast, during nonbanded periods, the mesoscale forcing is weaker and there is a clear increase in echo frequency and coverage over Tug Hill, leading to higher precipitation rates than found over the upstream lowlands. Even during these periods, however, there is no evidence of an increase in convective vigor as one moves inland over Tug Hill. Instead, other factors must explain the shift in frequency and coverage of radar echoes and precipitation during these periods. Possibilities include 1) the broadening of precipitating clouds due to decreased entrainment as the air mass lifts and moistens over elevated terrain (e.g., Kirshbaum and Grant 2012); 2) a vapor-diffusional seeder–feeder effect whereby increased cloud liquid water generated by gradual, forced

ascent acts as a feeder to the existing hydrometeors with ice growing via diffusional growth at the expense of the additional supercooled liquid water (e.g., Choularton and Perry 1986); 3) a reduction in low-level sublimation due to the decreased distance between ground and cloud base and moistening by ascent (e.g., Murakami et al. 1994); 4) an increase in precipitation efficiency as precipitation processes transition from convective to stratiform, as observed in mesoscale convective systems (e.g., Yuter and Houze 1995); and (5) the favorable downstream transport of hydrometeors generated near Lake Ontario to Tug Hill, as seen in numerical simulations in other lake-effect regions (e.g., Alcott and Steenburgh 2013).

Although not examined in depth, the transect mode periods classified as other had an overall orographic ratio of 3.2 and accounted for 6.6 h of the study period. During many of these periods, the large increase in precipitation between SC and NR occurred because a LLAP band was either aligned at an angle to the transect—missing SC entirely or only weakly covering it—or the transect was under or near the edge of a LLAP band or a weak band embedded in overall broad coverage, precluding classification of transect mode. The inland broadening of LLAP bands and/or the more persistent and widespread coverage over Tug Hill made it more likely for Tug Hill locations to observe precipitation during these periods, ultimately contributing to the overall enhancement observed during the event.

7. Conclusions

We have described how the ratio of upland to lowland precipitation (orographic ratio) east of Lake Ontario and over Tug Hill varied with the lake-effect precipitation mode during IOP2b of the Ontario Winter Lake-effect Systems (OWLeS) field campaign. During the primary 24-h study period (0000 UTC 11 December–0000 UTC 12 December 2013), precipitation fell over a relatively narrow swath extending from eastern Lake Ontario to over Tug Hill. Along the axis of maximum precipitation, total liquid precipitation equivalent increased from 33.5 mm at the lowland Sandy Creek observing site (SC; 145 m MSL) to 62.5 mm at the upland north Redfield observing site (NR; 385 m MSL) on the western slope of Tug Hill, the latter yielding 101.5 cm of snow.

Data collected along a transect of observing sites from the Lake Ontario shore to Tug Hill reveal that the highest precipitation and snowfall rates were produced by long-lake-axis parallel (LLAP) bands that accompanied the passage or approach of upper-level shortwave troughs. The strongest LLAP band period, which

occurred late in the event, occurred concurrently with the development of a surface trough over the Great Lakes region that appeared to contribute to convergence over Lake Ontario. When LLAP bands were aligned along the transect, however, the orographic ratio was small, with only a factor of 1.2 increase in precipitation from SC to NR. In addition, profiling radars showed a decrease in storm depth and convective vigor from the Lake Ontario shore to Tug Hill, in contrast to the convective invigoration described in contemporary models of lake-effect systems interacting with downstream terrain [e.g., Lackmann (2011), his Fig. 9.21]. We hypothesize that the strong mesoscale convergence associated with LLAP bands dominates the precipitation dynamics during these periods, resulting in high precipitation rates at both lowland and upland sites and a small increase in precipitation over Tug Hill.

In contrast, broad-coverage periods when nonbanded lake-effect precipitation impinged on the transect produced weaker overall precipitation rates but larger orographic ratios, with a factor of 2.3 increase in LPE from SC to NR and higher precipitation rates at NR compared to SC. During these periods, discontinuous, cellular convection over Lake Ontario and the adjoining lowlands transitioned to broader, more continuous echo coverage over Tug Hill. Although overall precipitation rates were lower, these periods account for almost half the study period (>10 h) and thus contributed strongly to the event-total precipitation maximum found over Tug Hill. Similar to banded periods, profiling radars revealed no evidence of an increase in the depth and vigor of convection over Tug Hill. Thus, even during these periods of large orographic ratio, mechanisms other than convective invigoration must be playing a role.

The lake-effect precipitation climatology east of Lake Ontario is dominated by broad-coverage periods, which account for 70% of lake-effect hours (Veals and Steenburgh 2015). While this study examines only one storm, we hypothesize that the climatological Tug Hill lake-effect precipitation maximum is produced primarily by the enhancement observed during broad-coverage periods. The weaker enhancement and broadening of LLAP bands plays a secondary role, although the intense precipitation rates associated with these bands remains a critical forecast concern in both lowland and upland areas.

Future work should utilize numerical modeling to investigate the processes controlling the distribution and intensity of precipitation east of Lake Ontario and variations in enhancement over Tug Hill. Improved knowledge and modeling of such storm characteristics is fundamental to advancing lake-effect prediction and can provide a valuable framework for forecasters in the region. While this study examined one representative lake-effect storm, a more comprehensive climatological study on the impacts of lake-effect mode on precipitation enhancement and distribution throughout the cool season is necessary. Additionally, we highlight the need to investigate the controls and formation mechanisms of lake-effect precipitation mode, which would aid the forecasting of lake-effect precipitation distributions and amounts.

REFERENCES

Alcott, T. I., and W. J. Steenburgh, 2013: Orographic influences on a Great Salt Lake–effect snowstorm. *Mon. Wea. Rev.*, **141**, 2432–2450, doi:10.1175/MWR-D-12-00328.1.

——, ——, and N. F. Laird, 2012: Great Salt Lake–effect precipitation: Observed frequency, characteristics, and associated environmental factors. *Wea. Forecasting*, **27**, 954–971, doi:10.1175/WAF-D-12-00016.1.

Barnes, S. L., F. Caracena, and A. Marroquin, 1996: Extracting synoptic-scale diagnostic information from mesoscale models: The Eta model, gravity waves, and quasigeostrophic diagnostics. *Bull. Amer. Meteor. Soc.*, **77**, 519–528, doi:10.1175/1520-0477(1996)077<0519:ESSDIF>2.0.CO;2.

Benjamin, S. G., and Coauthors, 2016: A North American hourly assimilation and model forecast cycle: The Rapid Refresh. *Mon. Wea. Rev.*, doi:10.1175/MWR-D-15-0242.1, in press.

Bergeron, T., 1965: On the low-level redistribution of atmospheric water caused by orography. *Proc. Int. Cloud Physics*, Tokyo, Japan, Amer. Meteor. Soc., 96–100.

Braham, R. R., Jr., 1983: The Midwest snow storm of 8–11 December 1977. *Mon. Wea. Rev.*, **111**, 253–272, doi:10.1175/1520-0493(1983)111<0253:TMSSOD>2.0.CO;2.

Browning, K. H., F. F. Hill, and C. W. Pardoe, 1974: Structure and mechanism of precipitation and the effect of orography in wintertime warm sector. *Quart. J. Roy. Meteor. Soc.*, **100**, 309–330, doi:10.1002/qj.49710042505.

Byrd, G. P., R. A. Anstett, J. E. Heim, and D. M. Usinski, 1991: Mobile sounding observations of lake-effect snowbands in western and central New York. *Mon. Wea. Rev.*, **119**, 2323–2332, doi:10.1175/1520-0493(1991)119<2323:MSOOLE>2.0.CO;2.

Choularton, T. W., and S. J. Perry, 1986: A model of the orographic enhancement of snowfall by the seeder-feeder mechanism. *Quart. J. Roy. Meteor. Soc.*, **112**, 335–345, doi:10.1002/qj.49711247204.

Colle, B. A., Y. Lin, S. Medina, and B. F. Smull, 2008: Orographic modification of convection and flow kinematics by the Oregon Coast Range and Cascades during IMPROVE-2. *Mon. Wea. Rev.*, **136**, 3894–3916, doi:10.1175/2008MWR2369.1.

——, R. B. Smith, and D. A. Wesley, 2013: Theory, observations, and predictions of orographic precipitation. *Mountain Weather Research and Forecasting: Recent Progress and Current Challenges*, F. K. Chow, S. F. J. De Wekker, and B. J. Snyder, Eds., Springer Atmospheric Sciences, Springer Netherlands, 291–344.

Crum, T. D., R. L. Alberty, and D. W. Burgess, 1993: Recording, archiving, and using WSR-88D data. *Bull. Amer. Meteor. Soc.*, **74**, 645–653, doi:10.1175/1520-0477(1993)074<0645:RAAUWD>2.0.CO;2.

Eito, H., T. Kato, M. Yoshizaki, and A. Adachi, 2005: Numerical simulation of the quasi- stationary snowband observed over the southern coastal area of the Sea of Japan on 16 January 2001. *J. Meteor. Soc. Japan*, **83**, 551–576, doi:10.2151/jmsj.83.551.

Forbes, G. S., and J. H. Merritt, 1984: Mesoscale vortices over the Great Lakes in wintertime. *Mon. Wea. Rev.*, **112**, 377–381, doi:10.1175/1520-0493(1984)112<0377:MVOTGL>2.0.CO;2.

Fujiyoshi, Y., T. Endoh, T. Yamada, K. Tsuboki, Y. Tachibana, and G. Wakahama, 1990: Determination of a Z–R relationship for snowfall using a radar and high sensitivity snow gauges. *J. Appl. Meteor.*, **29**, 147–152, doi:10.1175/1520-0450(1990)029<0147:DOARFS>2.0.CO;2.

Gallus, W. A., Jr., N. A. Snook, and E. V. Johnson, 2008: Spring and summer severe weather reports over the Midwest as a function of convective mode: A preliminary study. *Wea. Forecasting*, **23**, 101–113, doi:10.1175/2007WAF2006120.1.

Gunn, K. L. S., and J. S. Marshall, 1958: The distribution with size of aggregate snowflakes. *J. Meteor.*, **15**, 452–461, doi:10.1175/1520-0469(1958)015<0452:TDWSOA>2.0.CO;2.

Hill, J. D., 1971: Snow squalls in the lee of Lakes Erie and Ontario. NOAA Tech. Memo. NWS ER-43, 20 pp.

Hjelmfelt, M. R., 1990: Numerical study of the influence of environmental conditions on lake-effect snowstorms over Lake Michigan. *Mon. Wea. Rev.*, **118**, 138–150, doi:10.1175/1520-0493(1990)118<0138:NSOTIO>2.0.CO;2.

——, 1992: Orographic effects in simulated lake-effect snowstorms over Lake Michigan. *Mon. Wea. Rev.*, **120**, 373–377, doi:10.1175/1520-0493(1992)120<0373:OEISLE>2.0.CO;2.

Houze, R. A., Jr., 1997: Stratiform precipitation in the tropics: A meteorological paradox? *Bull. Amer. Meteor. Soc.*, **78**, 2179–2196, doi:10.1175/1520-0477(1997)078<2179:SPIROC>2.0.CO;2.

——, 2012: Orographic effects on precipitating clouds. *Rev. Geophys.*, **50**, RG1001, doi:10.1029/2011RG000365.

Hozumi, K., and C. Magono, 1984: The cloud structure of convergent cloud bands over the Japan Sea in winter monsoon period. *J. Meteor. Soc. Japan*, **62**, 522–533.

Kelly, R. D., 1982: A single Doppler radar study of horizontal-roll convection in a lake-effect snow storm. *J. Atmos. Sci.*, **39**, 1521–1531, doi:10.1175/1520-0469(1982)039<1521:ASDRSO>2.0.CO;2.

——, 1984: Horizontal roll and boundary-layer interrelationships observed over Lake Michigan. *J. Atmos. Sci.*, **41**, 1816–1826, doi:10.1175/1520-0469(1984)041<1816:HRABLI>2.0.CO;2.

——, 1986: Mesoscale frequencies and seasonal snowfalls for different types of Lake Michigan snow storms. *J. Climate Appl. Meteor.*, **25**, 308–312, doi:10.1175/1520-0450(1986)025<0308:MFASSF>2.0.CO;2.

Kirshbaum, D. J., and A. L. M. Grant, 2012: Invigoration of cumulus cloud fields by mesoscale ascent. *Quart. J. Roy. Meteor. Soc.*, **138**, 2136–2150, doi:10.1002/qj.1954.

Klugmann, D., K. Heinsohn, and H.-J. Kirtzel, 1996: A low cost 24 GHz FM-CW Doppler radar rain profiler. *Contrib. Atmos. Phys.*, **69**, 247–253.

Kristovich, D. A. R., and N. F. Laird, 1998: Observations of widespread lake-effect cloudiness: Influences of lake surface temperature and upwind conditions. *Wea. Forecasting*, **13**, 811–821, doi:10.1175/1520-0434(1998)013<0811:OOWLEC>2.0.CO;2.

——, ——, and M. R. Hjelmfelt, 2003: Convective evolution across Lake Michigan during a widespread lake-effect snow event. *Mon. Wea. Rev.*, **131**, 643–655, doi:10.1175/1520-0493(2003)131<0643:CEALMD>2.0.CO;2.

Lackmann, G., 2011: *Midlatitude Synoptic Meteorology: Dynamics, Analysis, and Forecasting*. Amer. Meteor. Soc., 360 pp.

Laird, N. F., 1999: Observation of coexisting mesoscale lake-effect vortices over the western Great Lakes. *Mon. Wea. Rev.*, **127**, 1137–1141, doi:10.1175/1520-0493(1999)127<1137:OOCMLE>2.0.CO;2.

——, and D. A. Kristovich, 2004: Comparison of observations with idealized model results for a method to resolve winter lake-effect mesoscale morphology. *Mon. Wea. Rev.*, **132**, 1093–1103, doi:10.1175/1520-0493(2004)132<1093:COOWIM>2.0.CO;2.

——, D. A. R. Kristovich, and J. E. Walsh, 2003a: Idealized model simulations examining the mesoscale structure of winter lake-effect circulations. *Mon. Wea. Rev.*, **131**, 206–221, doi:10.1175/1520-0493(2003)131<0206:IMSETM>2.0.CO;2.

——, J. E. Walsh, and D. A. R. Kristovich, 2003b: Model simulations examining the relationship to lake-effect morphology to lake shape, wind direction, and wind speed. *Mon. Wea. Rev.*, **131**, 2102–2111, doi:10.1175/1520-0493(2003)131<2102:MSETRO>2.0.CO;2.

Maahn, M., and P. Kollias, 2012: Improved Micro Rain Radar snow measurements using Doppler spectra post-processing. *Atmos. Meas. Tech.*, **5**, 2661–2673, doi:10.5194/amt-5-2661-2012.

Magono, C., K. Kikuchi, T. Kimura, S. Tazawa, and T. Kasai, 1966: A study on the snowfall in the winter monsoon season in Hokkaido with special reference to low land snowfall. *J. Fac. Sci., Hokkaido Univ., Ser. 7*, **11**, 287–308.

Matsuura, S., K. Matsuyama, S. Asano, T. Okamoto, and Y. Takeuchi, 2005: Fluctuation of the seasonal snowpack in a mountainous area of the heavy-snow district in the warm-temperate zone of Japan. *J. Glaciol.*, **51**, 547–554, doi:10.3189/172756505781829052.

Minder, J. R., T. W. Letcher, L. S. Campbell, P. V. Veals, and W. J. Steenburgh, 2015: The evolution of lake-effect convection during landfall and orographic uplift as observed by profiling radars. *Mon. Wea. Rev.*, **143**, 4422–4442, doi:10.1175/MWR-D-15-0117.1.

Muller, R. A., 1966: Snowbelts of the Great Lakes. *Weatherwise*, **19**, 248–255, doi:10.1080/00431672.1966.10544204.

Murakami, M., T. L. Clark, and W. D. Hall, 1994: Numerical simulations of convective snow clouds over the Sea of Japan: 2-dimensional simulations of mixed-layer development and convective snow cloud formation. *J. Meteor. Soc. Japan*, **72**, 43–62.

Nakai, S., and T. Endoh, 1995: Observation of snowfall and airflow over a low mountain barrier. *J. Meteor. Soc. Japan*, **73**, 183–199.

Niziol, T. A., 1987: Operational forecasting of lake effect snowfall in western and central New York. *Wea. Forecasting*, **2**, 310–321, doi:10.1175/1520-0434(1987)002<0310:OFOLES>2.0.CO;2.

——, W. R. Snyder, and J. S. Waldstreicher, 1995: Winter weather forecasting throughout the eastern United States. Part IV: Lake effect snow. *Wea. Forecasting*, **10**, 61–77, doi:10.1175/1520-0434(1995)010<0061:WWFTTE>2.0.CO;2.

Onton, D. J., and W. J. Steenburgh, 2001: Diagnostic and sensitivity studies of the 7 December 1998 Great Salt Lake–effect snowstorm. *Mon. Wea. Rev.*, **129**, 1318–1338, doi:10.1175/1520-0493(2001)129<1318:DASSOT>2.0.CO;2.

Passarelli, R. E. J., and R. R. J. Braham, 1981: The role of the winter land breeze in the formation of Great Lake snow storms. *Bull. Amer. Meteor. Soc.*, **62**, 482–491, doi:10.1175/1520-0477(1981)062<0482:TROTWL>2.0.CO;2.

Peace, R. L., and R. B. Sykes, 1966: Mesoscale study of a lake effect snowstorm. *Mon. Wea. Rev.*, **94**, 495–507, doi:10.1175/1520-0493(1966)094<0495:MSOALE>2.3.CO;2.

Rasmussen, R., M. Dixon, S. Vasiloff, F. Hage, S. Knight, J. Vivekanandan, and M. Xu, 2003: Snow nowcasting using a real-time correlation of radar reflectivity with snow gauge accumulation. *J. Appl. Meteor.*, **42**, 20–36, doi:10.1175/1520-0450(2003)042<0020:SNUART>2.0.CO;2.

——, and Coauthors, 2012: How well are we measuring snow: The NOAA/FAA/NCAR winter precipitation test bed. *Bull. Amer. Meteor. Soc.*, **93**, 811–829, doi:10.1175/BAMS-D-11-00052.1.

Reinking, R. F., and Coauthors, 1993: The Lake Ontario Winter Storms (LOWS) project. *Bull. Amer. Meteor. Soc.*, **74**, 1828–1849, doi:10.1175/1520-0477-74-10-1828.

Roe, G. H., 2005: Orographic precipitation. *Annu. Rev. Earth Planet. Sci.*, **33**, 645–671, doi:10.1146/annurev.earth.33.092203.122541.

Saito, K., M. Murakami, T. Matsuo, and H. Mizuno, 1996: Sensitivity experiments on the orographic snowfall over the mountainous region of northern Japan. *J. Meteor. Soc. Japan*, **74**, 797–813.

Savina, M., B. Schäppi, P. Molnar, P. Burlando, and B. Sevruk, 2012: Comparison of a tipping-bucket and electronic weighing precipitation gage for snowfall. *Atmos. Res.*, **103**, 45–51, doi:10.1016/j.atmosres.2011.06.010.

Schroeder, J. J., D. A. R. Kristovich, and M. R. Hjelmfelt, 2006: Boundary layer and microphysical influences of natural cloud seeding on a lake-effect snowstorm. *Mon. Wea. Rev.*, **134**, 1842–1858, doi:10.1175/MWR3151.1.

Smith, R. B., 2006: Progress on the theory of orographic precipitation. Tectonics, climate, and landscape evolution, Geological Society of America Special Paper 398, 1–16, doi:10.1130/2006.2398(01).

——, P. Schafer, D. J. Kirshbaum, and E. Regina, 2009: Orographic precipitation in the tropics: Experiments in Dominica. *J. Atmos. Sci.*, **66**, 1698–1716, doi:10.1175/2008JAS2920.1.

Smith, T. L., S. G. Benjamin, J. M. Brown, S. Weygandt, T. Smirnova, and B. Schwartz, 2008: Convection forecasts from the hourly updated, 3-km high resolution Rapid Refresh (HRRR) model. *24th Conf. on Severe Local Storms*, Savannah, GA, Amer. Meteor. Soc., 11.1. [Available online at https://ams.confex.com/ams/24SLS/webprogram/Paper142055.html.]

Steenburgh, W. J., and D. J. Onton, 2001: Multiscale analysis of the 7 December 1998 Great Salt Lake–effect snowstorm. *Mon. Wea. Rev.*, **129**, 1296–1317, doi:10.1175/1520-0493(2001)129<1296:MAOTDG>2.0.CO;2.

——, S. F. Halvorson, and D. J. Onton, 2000: Climatology of lake-effect snowstorms of the Great Salt Lake. *Mon. Wea. Rev.*, **128**, 709–727, doi:10.1175/1520-0493(2000)128<0709:COLESO>2.0.CO;2.

Steiger, S. M., and Coauthors, 2013: Circulations, bounded weak echo regions, and horizontal vortices observed within long-lake-axis-parallel–lake-effect storms by the Doppler on Wheels. *Mon. Wea. Rev.*, **141**, 2821–2840, doi:10.1175/MWR-D-12-00226.1.

Stoelinga, M. T., R. E. Stewart, G. Thompson, and J. Theriault, 2013: Microphysical processes within winter orographic cloud and precipitation systems. *Mountain Weather Research and Forecasting: Recent Progress and Current Challenges*, F. K. Chow, S. F. J. De Wekker, and B. J. Snyder, Eds., Springer Atmospheric Sciences, Springer Netherlands, 345–408.

Vasiloff, S., 2001: WSR-88D performance in northern Utah during the winter of 1998–1999. Part I: Adjustments to precipitation estimates. NOAA/Western Regional Tech. Attachment 01-03, 5 pp.

Veals, P. G., and W. J. Steenburgh, 2015: Climatological characteristics and orographic enhancement of lake-effect precipitation east of Lake Ontario and over the Tug Hill Plateau. *Mon. Wea. Rev.*, **143**, 3591–3609, doi:10.1175/MWR-D-15-0009.1.

Weckwerth, T. M., J. W. Wilson, R. M. Wakimoto, and N. A. Crook, 1997: Horizontal convective rolls: Determining the environmental conditions supporting their existence and characteristics. *Mon. Wea. Rev.*, **125**, 505–526, doi:10.1175/1520-0493(1997)125<0505:HCRDTE>2.0.CO;2.

Welsh, D., B. Geerts, J. R. Minder, W. J. Steenburgh, and P. T. Bergmaier, 2015: The quest to understand heavy lake-effect snowfall from long-lake-axis-parallel snow bands: Multi-frequency reflectivity profiles of the 11 December 2013 band over and downwind of Lake Ontario. *16th Conf. on Mesoscale Processes*, Boston, MA, Amer. Meteor. Soc., P8.7. [Available online at https://ams.confex.com/ams/16Meso/webprogram/Paper274322.html.]

Wüest, M., C. Frei, A. Altenhoff, M. Hagen, M. Litschi, and C. Schar, 2010: A gridded hourly precipitation dataset for Switzerland using rain-gauge analysis and radar-based disaggregation. *Int. J. Climatol.*, **30**, 1764–1775.

Yamada, Y., M. Murakami, H. Mizuno, M. Maki, S. Nakai, and K. Iwanami, 2010: Kinematic and thermodynamical structures of longitudinal-mode snow bands over the Sea of Japan during cold-air outbreaks Part I: Snow bands in large vertical shear environment in the band-transverse direction. *J. Meteor. Soc. Japan*, **88**, 673–718, doi:10.2151/jmsj.2010-404.

Yeager, K. N., W. J. Steenburgh, and T. I. Alcott, 2013: Contributions of lake-effect periods to the cool-season hydroclimate of the Great Salt Lake basin. *J. Appl. Meteor. Climatol.*, **52**, 341–362, doi:10.1175/JAMC-D-12-077.1.

Yuter, S., and R. A. Houze, 1995: Three-dimensional kinematic and microphysical evolution of Florida cumulonimbus. Part II: Frequency distributions of vertical velocity, reflectivity, and differential reflectivity. *Mon. Wea. Rev.*, **123**, 1941–1963, doi:10.1175/1520-0493(1995)123<1941:TDKAME>2.0.CO;2.

Zhang, J., and Coauthors, 2016: Multi-Radar Multi-Sensor (MRMS) quantitative precipitation estimation: Initial operating capabilities. *Bull. Amer. Meteor. Soc.*, doi:10.1175/BAMS-D-14-00174.1, in press.